

Reprinted (adapted) with permission from The Journal of Physical Chemistry A, *Collision Dynamics of O(³P) + DMMP Using a Specific Reaction Parameter Potential Form*, P.F. Conforti et al., American Chemical Society, March 15, 2012.

Collision Dynamics of O(³P) + DMMP Using a Specific Reaction Parameters Potential Form

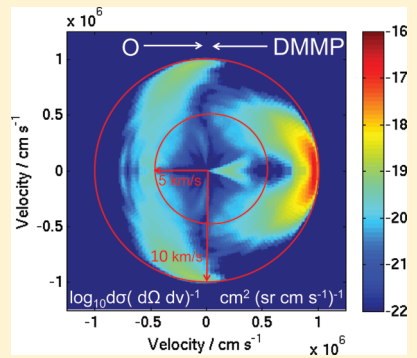
Patrick F. Conforti and Matthew Braunstein*

Spectral Sciences, Inc., 4 Fourth Avenue, Burlington, Massachusetts 01803, United States

Jaime A. Stearns and James A. Dodd

Air Force Research Laboratory, Kirtland AFB, New Mexico 87117, United States

ABSTRACT: Starting from previous benchmark CBS-QB3 electronic structure calculations (Conforti, P. F.; Braunstein, M.; Dodd, J. A. *J. Phys. Chem. A* **2009**, *113*, 13752), we develop two global potential energy surfaces for O(³P) + DMMP collisions, using the specific reaction parameters approach. Each surface is simultaneously fit along the three major reaction pathways: hydrogen abstraction, hydrogen elimination, and methyl elimination. We then use these surfaces in classical dynamics simulations and compute reactive cross sections from 4 to 10 km s⁻¹ collision velocity. We examine the energy disposal and angular distributions of the reactive and nonreactive products. We find that for reactive collisions, an unusually large amount of the initial collision energy is transformed into internal energy. We analyze the nonreactive and reactive product internal energy distributions, many of which fit Boltzmann temperatures up to \sim 2000 K.



I. INTRODUCTION

The proliferation of weapons of mass destruction, including chemical warfare agents, has renewed interest in the fundamental chemistry of nerve agents such as sarin and VX and their main simulant, dimethyl methylphosphonate (DMMP).^{1–8} For example, recent studies have examined the interaction of DMMP with surfaces, including reactivity and decomposition on TiO₂¹ and silica.² There have also been recent investigations on gas phase decomposition mechanisms and reaction rate kinetics of DMMP.^{3,8,9} In the present work, we focus on the interaction of DMMP with atomic oxygen, O(³P), which is important in assessing chemical interactions of nerve agents released in the upper atmosphere, where O(³P) is a major species.

In our initial study of O(³P) collisions with sarin and the simulant DMMP,⁵ we characterized the main stationary points and reaction pathways with several levels of theory, including semiempirical, density functional, and benchmark CBS-QB3. For these systems, we found three major pathways. For O(³P) + DMMP, the focus of the present work, the three pathways are shown in Figure 1: hydrogen abstraction to create OH (reactions 1 and 2), the elimination of hydrogen following O(³P) addition (reactions 3 and 4), and the elimination of a methyl radical following O(³P) addition (reactions 5 and 6). The hydrogen abstraction reactions have relatively low reaction barriers less than 10 kcal mol⁻¹ and reaction enthalpies that are within 5 kcal mol⁻¹ of thermoneutral. In contrast, the elimination reactions have barriers greater than 40 kcal mol⁻¹ and reaction enthalpies that range from approximately -15 to +35 kcal mol⁻¹. These characteristics have a great deal in common with O(³P) plus small-chain hydrocarbon systems,

which also have comparable reactive channels, transition states, and reaction energies.^{10–12}

Starting from our previous work on the O(³P) + DMMP and O(³P) + sarin systems, in the present paper we develop two global potential energy surfaces for O(³P) + DMMP collisions, using the specific reaction parameters (SRP) approach.¹³ Truhlar and co-workers initially developed the SRP method, where semiempirical potential parameters were tuned in order to examine a reaction of interest, and then direct dynamics were performed using the modified semiempirical parameters. As many groups have done since the seminal work of Truhlar, we adopt the SRP approach and use it to examine the O(³P) + DMMP potential surface. Each of the global surfaces is simultaneously fit using benchmark CBS-Q electronic structure calculations along the three major reaction pathways. We then use these surfaces in classical dynamics simulations. We compute the cross sections for the major O(³P) + DMMP reaction pathways, from 4 to 10 km s⁻¹ collision velocity. We then examine the energy disposal and angular distributions of the reactive and nonreactive products. We find that for reactive collisions, an unusually large amount of the initial collision energy is transformed into internal energy. For example, for H-atom elimination at 8 km s⁻¹ collision velocity, on average about 80% of the available energy goes into internal energy of the product DMMP-O radical. This percentage is larger than comparable hyperthermal reactions¹⁴ and many chemical interactions in general. For CH₃ elimination, about 60–70%

Received: October 26, 2011

Revised: January 13, 2012

Published: January 27, 2012

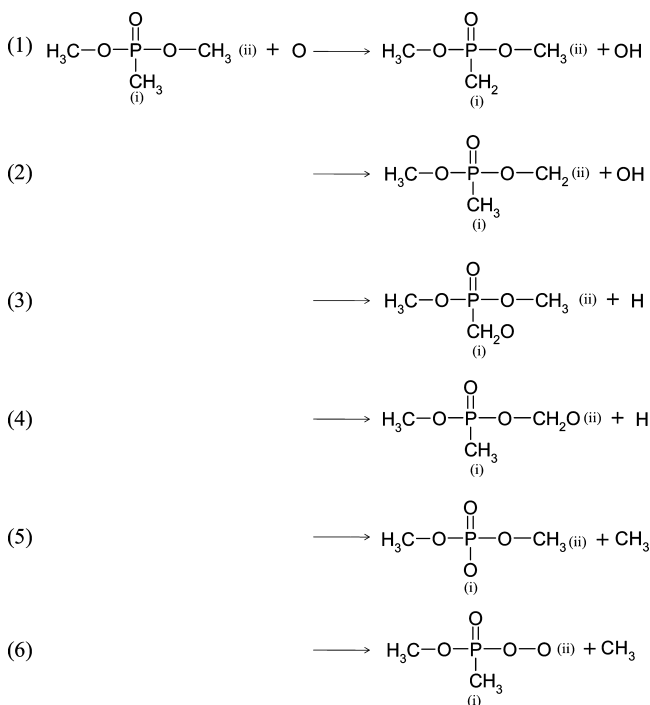


Figure 1. Major collisional reactions for DMMP + O(³P): (1) and (2) hydrogen abstraction; (3) and (4) hydrogen elimination; (5) and (6) methyl elimination.

goes into internal energy of products, and for H-atom abstraction between 50 and 60% goes into product internal energy. The internal energy deposition is correlated with the distribution of impact parameters: nearly all H-elimination reactions are “hard collisions” with impact parameters less than 1.0 Å. Nearly all CH₃ elimination reactions occur for impact parameters less than 2 Å, and the H-atom abstraction pathway has a broad range of impact parameters up to about 3 Å. Nonreactive collisions result in a wide range of product internal energies, which can be separated into forward and backward scattering mechanisms. We further analyze the nonreactive and reactive product internal energy distributions, many of which fit Boltzmann temperatures up to ~2000 K, and predict excited product spectra.

Hyperthermal O-atom beams have recently been used to investigate O(³P) + small-chain hydrocarbon reactions,^{10,11,15,16} and there have been recent studies which use SRP potentials to examine these same systems.^{12,17} As we are not aware of any other efforts examining hyperthermal collisions of O(³P) with DMMP or other nerve agents or simulants, the present results provide guidance for possible future measurements in this area. Furthermore, the present results extend the use of SRP potentials to larger hydrocarbon systems and give insight into the unusual hyperthermal collision dynamics of medium-sized hydrocarbon molecules.

The paper proceeds as follows. Section II describes benchmark electronic structure calculations performed on the O(³P) + DMMP system and the construction of two separate global potential energy surfaces using the SRP potential form. The construction of two potential surfaces, which use slightly different cost functions, is useful as it gives some indication of the sensitivity of the cross sections and other dynamical quantities to errors in the surface. The surfaces are compared to semiempirical potentials and to the benchmark calculations

from which they were derived. Section III describes O(³P) + DMMP classical dynamics calculations using the two SRP surfaces. Reaction cross sections are given, and product internal energies and angular distributions are analyzed. Section IV gives conclusions.

II. AM1 SRP POTENTIAL

Although there have been great strides in developing accurate, multidimensional, global potential energy surfaces,^{18–24} molecules with more than approximately six atoms remain a challenge, principally due to the large number of degrees of freedom involved and the possibility of multiple reaction pathways. Recently the SRP method has been developed and successfully applied to hyperthermal reaction systems containing five to nine atoms.^{12,17} The idea is to start with a semiempirical potential and adjust the parameters to match properties of known experimental values and/or high-order electronic structure calculations for a particular process or reaction. The fast-running, full degree of freedom properties of the semiempirical method are retained, but the SRP surface provides accuracy comparable to the potential surface data used in the reparameterization. The challenge of this method is to optimize the semiempirical parameters in such a way that key features of the surface are improved to a satisfactory degree, without introducing deficiencies and artifacts.

We seek to optimize a single semiempirical potential which simultaneously describes all three pathways (six reactions of Figure 1) for O(³P) + DMMP collisions. We chose a procedure that has been used for other smaller systems, including alkane rearrangement reactions,^{25,26} hyperthermal O(³P) + alkane reactions,^{12,17} and hyperthermal F + alkane reactions.²⁷ We start with an AM1 potential. We interfaced the nonlinear least-squares solver MINPACK²⁸ with the GAMESS computational chemistry package.²⁹ While other algorithms for nonlinear optimization of semiempirical parameters have been utilized, such as genetic algorithms,^{12,30} the Levenberg–Marquardt algorithm as implemented in MINPACK also performs well in optimizing parameters.^{17,31} For optimization of the AM1 parameters, we chose a set of relevant structures. In particular, the reactants, products, and transition states as shown in Figure 1 of ref 5, and their energies and gradients at the CBS-QB3 level are used. The combustion study of Tester and co-workers showed that the differences between the ab initio calculations using CBS-Q of the heat of formation for organophosphorus compounds were within 2.5 kcal mol⁻¹ of the literature values where available.³² Therefore, we use this level of theory as the benchmark for the optimization calculations. Additionally, starting from the transition structures, we used 10 points (energies and gradients) in both the forward and reverse directions along the intrinsic reaction coordinate using B3LYP/CBSB7, which is the initial calculation for the compound CBS-QB3 method used in ref 5. GAMESS performs the semiempirical calculations and MINPACK adjusts AM1 parameters on the relevant atoms (P, C, H, and O) using the least-squares cost function

$$w_E \sum_i (E_i^{\text{AM1}} - E_i^{\text{CBS}})^2 + w_L \sum_i (L_i^{\text{AM1}} - L_i^{\text{CBS}})^2$$

where E_i and L_i are the energy and gradient magnitudes, respectively, of geometry i with weighting w_E and w_L . For these calculations, w_E is set to 1.0 (mol kcal⁻¹)² and w_L is set at 50.0 (mol Å kcal⁻¹)². For phosphorus, oxygen, and carbon, 12 AM1

Table 1. AM1 and AM1-SRP Parameters for H, C, O, and P Atoms

parameter	H			C		
	AM1	AM1-SRP1	AM1-SRP2	AM1	AM1-SRP1	AM1-SRP2
U_{ss}	-11.3964	-11.7606	-11.7423	-52.0287	-51.5477	-51.5311
U_{pp}				-39.6142	-38.8044	-38.7211
β_s	-6.1738	-6.2808	-6.2837	-15.7158	-16.0314	-16.0471
β_p				-7.7193	-7.8639	-7.8835
ζ_s	1.1881	1.1725	1.1704	1.8087	1.7612	1.7596
ζ_p				1.6512	1.6749	1.6732
α	2.8823	2.9116	2.9129	2.6483	2.6402	2.6402
G_{ss}	12.8480	12.8918	12.9121	12.2300	12.8842	12.8535
G_{sp}				11.1400	11.8874	11.8968
G_{pp}				11.0800	10.6964	10.7772
G_{p2}				9.8400	10.1710	10.1809
H_{sp}				2.4300	2.4988	2.4854
parameter	O			P		
	AM1	AM1-SRP1	AM1-SRP2	AM1	AM1-SRP1	AM1-SRP2
U_{ss}	-97.8300	-98.7177	-98.5818	-42.0299	-42.4211	-42.4248
U_{pp}	-78.2624	-78.2643	-78.2622	-34.0307	-34.5494	-34.5681
β_s	-29.2728	-28.9311	-28.8875	-6.3538	-6.3010	-6.2943
β_p	-29.2728	-29.1341	-29.1139	-6.5907	-6.2516	-6.2376
ζ_s	3.1081	3.1540	3.1592	1.9813	2.0817	2.0883
ζ_p	2.5240	2.5107	2.5100	1.8752	1.9499	1.9548
α	4.4537	4.4333	4.4450	2.4553	2.4650	2.4656
G_{ss}	15.4200	14.9095	14.8658	11.5600	11.4228	11.4388
G_{sp}	14.4800	14.3813	14.3836	5.2374	5.0413	5.0344
G_{pp}	14.5200	14.5104	14.5002	7.8776	7.1561	7.1431
G_{p2}	12.9800	12.9777	12.9780	7.3076	6.9030	6.8879
H_{sp}	3.9400	3.9528	3.9447	0.7792	0.7515	0.7508

parameters are optimized, and for hydrogen 5 AM1 parameters are optimized. Therefore there are 41 (12*(phosphorus, oxygen, and carbon) + 5 hydrogen) AM1 parameters fit with a total of 320 data points: 23 geometries*2(energy + gradient magnitude) for reactions 1–4 and 6, plus 45 geometries*2-(energy + gradient magnitude) for reaction 5. To understand the sensitivity of the resulting SRP potential to the fitting method, two AM1-SRP potentials were determined using the above procedure (labeled AM1-SRP1 and AM1-SRP2). For the AM1-SRP1 potential, all six reactions were used at one time to reparameterize the AM1 parameters. For the AM1-SRP2 potential, AM1 parameters were optimized sequentially. First the abstraction reactions were optimized, followed by the hydrogen elimination reactions, and finally the methyl elimination reactions. During the optimization, the parameters were allowed to vary within 10% of their original values. A comparison of the AM1 parameters is given in Table 1 for the H, C, O, and P atoms. The average percent change between the SRP and original AM1 parameters is approximately 2.2%, with a maximum change of 9.3%.

Table 2 compares the energies of the stationary points and transition structures for the $O(^3P)$ + DMMP reactions using CBS-QB3, which is considered benchmark, and the unmodified AM1, AM1-SRP1, and AM1-SRP2 potentials. All energies are referenced to the $O(^3P)$ + DMMP reactant asymptote, and the units for all energies are kcal mol⁻¹. The CBS-QB3 calculations are performed using the Gaussian03 computational chemistry package,³³ and the AM1 semiempirical calculations are performed using the GAMESS package.²⁹ One major deficiency of the AM1 potential is that the reaction energies are more exothermic than the CBS-QB3 results, particularly for the

hydrogen abstraction reaction. This problem is largely corrected with the SRP potentials. In fact, the SRP2 potential for reaction 2 reproduces the CBS-QB3 results well for the barrier and reaction energies. However, the SRP2 improvement is modest at best for hydrogen elimination, while SRP1 does well for hydrogen elimination reaction 4. For methyl elimination, the SRP potentials improve the initial barrier for reaction 5 and the barrier for reaction 6, but for some of the reaction energies, the SRP potentials are slightly more exothermic than AM1. This degree of optimization with the SRP potentials is similar to recent studies for $O(^3P)$ + hydrocarbons.^{12,17} For instance, in Yan et al., two semiempirical SRP potential sets were examined for the $O(^3P)$ + ethane system, where either 6 or 12 reactions on the energy surface are used for the reparameterization.¹² The agreement between the SRP results and the high-level MRCI calculations for the activation barriers and reaction energies span from approximately 0 to 16 kcal mol⁻¹. This shows the level of agreement for a diverse reaction set and is similar to what is achieved with the present study. As will be shown, the dynamical results for SRP1 and SRP2 generally agree well with each other and are much less reactive than the AM1 results, especially near thresholds. This indicates that the optimization procedures have qualitatively changed the AM1 potential and that dynamically the SRP1 and SRP2 potentials are behaving in a similar way.

To compare the potential surfaces, we calculate the absolute error for the semiempirical surfaces using discrete points along the reaction pathway for each reaction compared to the B3LYP/CBSB7 reaction surfaces. These points are computed using the transition state geometry and scanning those bonds

Table 2. Reaction Barriers (ΔE^\ddagger) and Enthalpies (ΔE) in kcal mol⁻¹ of the O(³P) + DMMP Reactions Calculated at 0 K Including Zero-Point Energy^a

reaction	ΔE^\ddagger			ΔE				
	AM1	AM1-SRP1	AM1-SRP2	CBS-QB3	AM1	AM1-SRP1	AM1-SRP2	CBS-QB3
O + C ₃ H ₉ O ₃ P → OH + C ₃ H ₈ O ₃ P(i)	(1)	18.1	21.7	17.3	8.2	-23.3	-2.8	-4.6
O + C ₃ H ₉ O ₃ P → OH + C ₃ H ₈ O ₃ P(ii)	(2)	11.4	16.6	8.3	3.2	-32.0	-11.7	-4.6
O + C ₃ H ₉ O ₃ P → H + C ₃ H ₈ O ₄ P(i)	(3)	46.6	51.8	39	44.2	4.5	12.4	14.2
O + C ₃ H ₉ O ₃ P → H + C ₃ H ₈ O ₄ P(ii)	(4)	34.1	41.9	28.1	41.0	-13.2	2.9	-11.4
O + C ₃ H ₉ O ₃ P → Int → CH ₃ + C ₂ H ₆ O ₄ P(i)	(5)	26.2/4.6	41.8/24.5	32.8/15.6	69.4/9.0	-1.6/-24.0	10.2/-12.6	10.0/-30.0
O + C ₃ H ₉ O ₃ P → CH ₃ + C ₂ H ₆ O ₄ P(ii)	(6)	60.7	55.2	52.6	44.8	25.7	21.4	29.4

^aWe note that reaction 5 proceeds through an intermediate (Int) as discussed in ref 5.

that are breaking/forming for a particular reaction while leaving the remaining degrees of freedom at their initial geometry. Histograms of the absolute errors for points along the minimum energy for all reactions are given in Figure 2a for the nonoptimized AM1 (black), the AM1-SRP1 (red), and the AM1-SRP2 (blue). From this plot, the original AM1 potential leads to frequent errors of approximately 12.5–17.5 kcal mol⁻¹. Many of these errors are in the product channels where the AM1 is overly exothermic. Both the AM1-SRP1 and AM1-SRP2 decrease the large errors associated with the AM1; however, the AM1-SRP2 does have several large errors (greater than 20 kcal mol⁻¹). The overall mean absolute error (MAE) for the nonoptimized AM1 is 8.6 kcal mol⁻¹, while the MAEs for SRP1 and SRP2 are 8.0 and 8.2 kcal mol⁻¹, respectively. The best improvement occurs for the hydrogen abstraction reactions which dominate the dynamics at lower velocities. In Figure 2b, histograms are given for the hydrogen abstraction reaction for the nonoptimized AM1 (black), the AM1-SRP1 (red), and the AM1-SRP2 (blue). Similarly, the large error between 12.5 and 17.5 kcal mol⁻¹ for the original AM1 potential is due to the large exothermic inaccuracy for these reactions (as shown in Table 2). Additionally, the AM1-SRP2 shows the best improvement along the hydrogen abstraction reaction pathways. For this reaction, the MAE decreases from 8.7 kcal mol⁻¹ for the original, unmodified AM1 to 5.8 and 3.6 kcal mol⁻¹ for the SRP1 and SRP2, respectively. To get more of a sense of the errors in the surfaces, contour plots of the hydrogen abstraction reaction 1 are given in Figure 3 and plots of the hydrogen abstraction reaction 2 are given in Figure 4 for each level of theory. The overall correction of the overly large AM1 exothermicities is clearly seen in the reparameterized surfaces.

III. MOLECULAR DYNAMICS SIMULATIONS

Classical molecular dynamics simulations of O(³P) + DMMP collisions are performed using the dynamic reaction path (DRC) routine within the GAMESS computational chemistry package.²⁹ The potential is calculated as the simulation progresses using both AM1-SRP1 and AM1-SRP2 potentials. For reference, we also include results using the standard, unmodified (non-SRP) AM1 potential. Procedures follow those of ref 5. The integration time step was 0.1 fs using the velocity-verlet integrator, the initial separation between fragments was 15 Å, final separation to products was 18 Å, the SCF convergence criterion was 1.0×10^{-5} hartree, and the maximum tolerance for the deviation for energy conservation (per step) is set to 5.0×10^{-5} hartree. Collision velocities of 4, 6, 8, and 10 km s⁻¹ are examined. This velocity range overlaps with recently reported hyperthermal measurement capabilities³⁴ and also overlaps the relative collision velocity of outgassed molecules from spacecraft and the atmospheric wind at altitudes of 150–700 km.³⁵ At each collision velocity and for each surface (the standard AM1, AM1-SRP1, AM1-SRP2), 10 000 trajectories are calculated. For a given collision velocity, at most 40 trajectories per 10 000 do not meet the maximum energy tolerance and are discarded. To start a trajectory, the minimum energy structures of DMMP are randomly oriented using Euler angles and a random impact parameter is chosen. Initial internal DMMP velocities are determined from the zero-point energy through normal-mode sampling with zero initial rotational energy. The maximum impact parameter is set at 4.1 Å. Examination of the opacity function has shown this to be an acceptable cutoff value. Most of the trajectories are run for

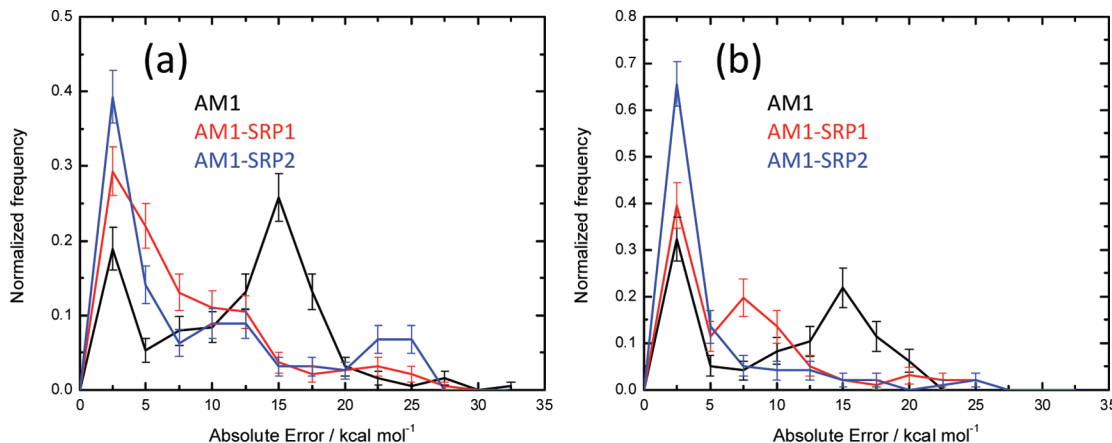


Figure 2. Histograms of the absolute errors for points along the energy reaction pathways for (a) all reactions and (b) hydrogen abstraction reactions. The AM1 results are shown in black, the AM1-SRP1 results are shown in red, and the AM1-SRP2 results are shown in blue. Error bars indicate standard deviation, and the energy bin size is 2.5 kcal mol⁻¹.

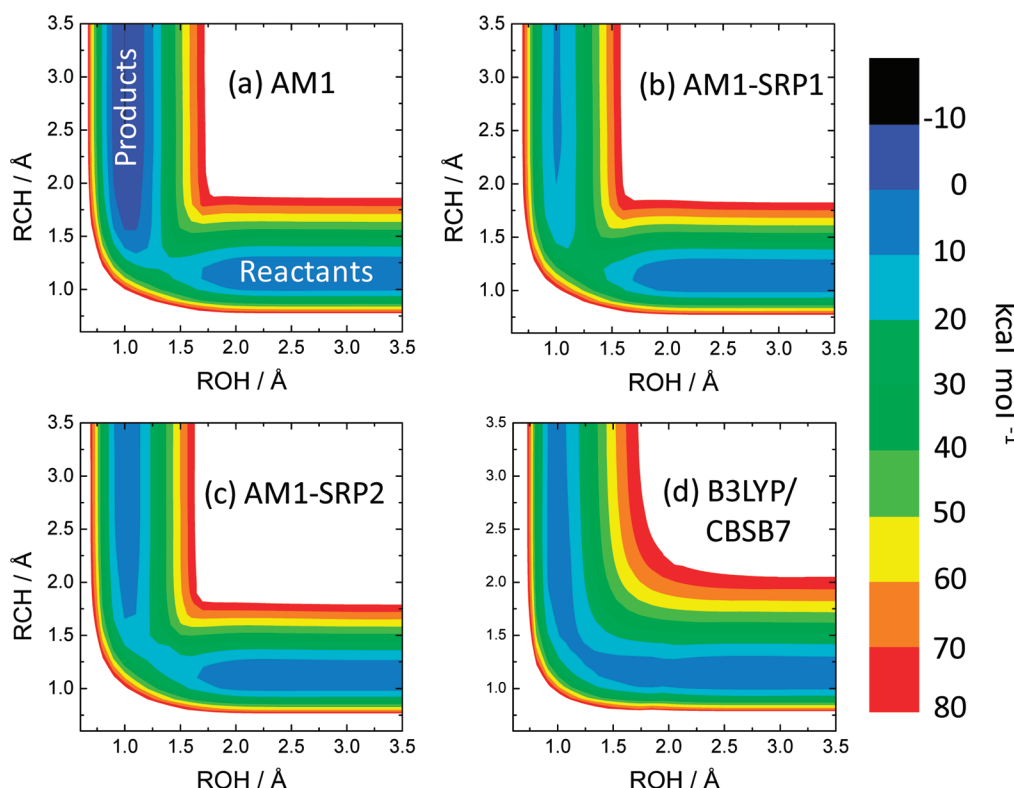


Figure 3. Surface contours for the hydrogen abstraction reaction 1 using (a) AM1, (b) AM1-SRP1, (c) AM1-SRP2, and (d) B3LYP/CBSB7. The energies are given in relation to the DMMP + O(³P) reactant asymptote.

several hundred femtoseconds to one picosecond to assess the primary collision interaction process and resulting reaction products.

The total cross section as a function of collision velocity is shown in Figure 5 for each pathway. In the plot and in the following discussion, the two reactions for each pathway are summed, so that reactions 1 and 2 of Figure 1 are summed to give the H-abstraction cross section, reactions 3 and 4 give the H-elimination cross section, and reactions 5 and 6 give the CH₃ elimination cross section. Three results are shown using the three different potentials, AM1 which we reported on previously,⁵ SRP1, and SRP2. In general, both AM1-SRP cross sections are similar to each other and are lower than the

original AM1 cross sections previously calculated, particularly the H-abstraction and CH₃ elimination pathways. The major correction of the SRP potentials is to decrease the reaction exothermicity and to generally increase the potential energy after the barrier region in the product channels. The increase in the potential in this way makes it less likely that a given trajectory will proceed to separated products. Focusing on the individual reactive pathway SRP cross sections, the H-atom abstraction reaction has a significant cross section at low collision velocities, as might be expected by the relatively low reaction barriers. The hydrogen elimination reaction becomes competitive with the abstraction reaction at 8 km s⁻¹ when the available collision energy (~ 108 kcal mol⁻¹) is well above the

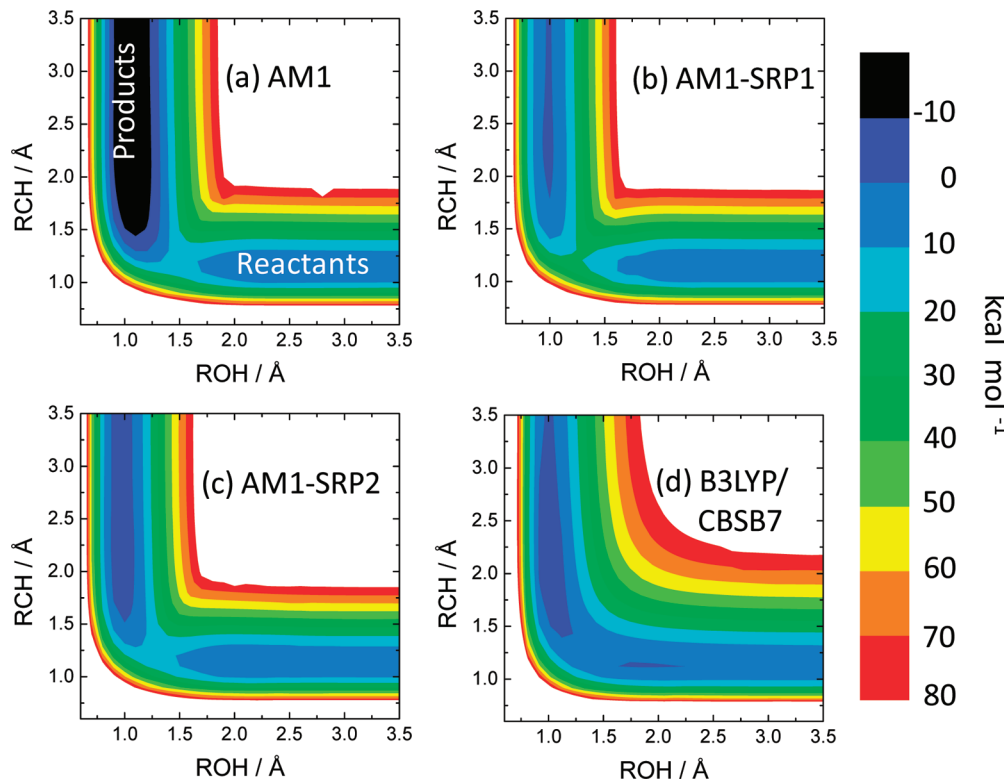


Figure 4. Surface contours for the hydrogen abstraction reaction 2 using (a) AM1, (b) AM1-SRP1, (c) AM1-SRP2, and (d) B3LYP/CBSB7. The energies are given in relation to the DMMP + O(³P) reactant asymptote.

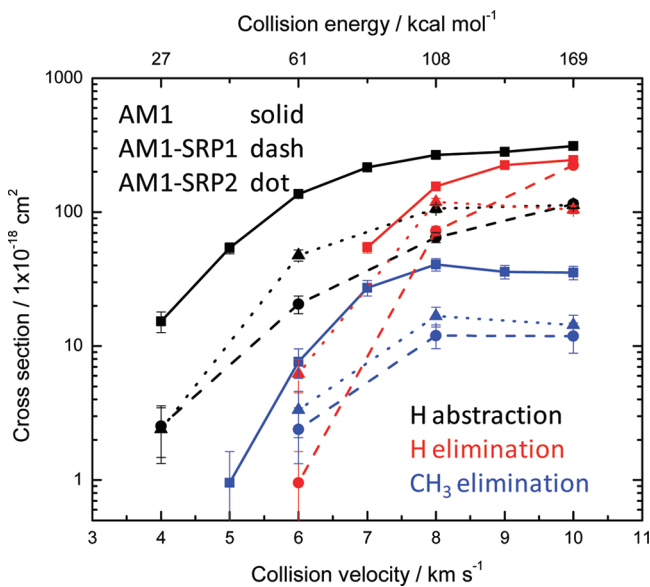


Figure 5. Reaction cross section as a function of collision velocity (km s⁻¹) and energy (kcal mol⁻¹) for the hydrogen abstraction (black), hydrogen elimination (red), and methyl elimination (blue) reactions. The AM1 results are shown with the solid lines and square symbols; the AM1-SRP1 results are shown with dashed lines and circular symbols; the AM1-SRP2 results are shown with dotted lines and triangular symbols. Error bars indicate standard deviation.

reaction barrier. At lower collision velocities, the hydrogen and methyl elimination pathways are comparable. The H-elimination cross sections grow much more rapidly with collision velocity than CH₃ elimination, so that at 10 km s⁻¹, H-elimination is about 10 times more likely than CH₃ elimination.

Some of this difference is due to the fact that there are three times as many available hydrogen atoms as methyl groups.

The distribution of energy in the collided O(³P) + DMMP products has not been previously explored. The product energies will be important in guiding product detection schemes for possible hyperthermal beam measurements. These distributions are also of fundamental importance in understanding the collision dynamics of O-atom with medium-sized hydrocarbon molecules. Tables 3–5 present an overview

Table 3. Average Total Vibrational Energy (E_{vib}) Excluding Zero-Point, Rotational (E_{rot}), and Relative Translational Energy (E_{trans}), in kcal mol⁻¹ for the Products of the Hydrogen Abstraction Pathway^a

velocity (km s ⁻¹)	potential	H abstraction		
		$\langle E_{\text{vib}} \rangle$	$\langle E_{\text{rot}} \rangle$	$\langle E_{\text{trans}} \rangle$
8	AM1	52.1 (0.35)	40.8 (0.27)	56.7 (0.38)
	AM1-SRP1	47.5 (0.36)	38.7 (0.29)	48.2 (0.36)
	AM1-SRP2	34.7 (0.27)	32.7 (0.25)	63.0 (0.48)
10	AM1	59.8 (0.28)	48.9 (0.23)	104.7 (0.49)
	AM1-SRP1	58.0 (0.28)	51.0 (0.25)	94.9 (0.46)
	AM1-SRP2	45.8 (0.24)	40.3 (0.21)	107.8 (0.55)

^aThe fraction of the total energy (initial translational energy + the average of the reaction enthalpies) is given in parentheses.

of the product energy deposition for the hydrogen abstraction, hydrogen elimination, and methyl elimination pathways, respectively. The average vibrational (excluding zero-point), rotational, and relative translational energies for each pathway are given at collision velocities of 8 and 10 km s⁻¹. As in the discussion of the cross sections, results for the two channels of

Table 4. Average Total Vibrational Energy (E_{vib}) Excluding Zero-Point, Rotational (E_{rot}), and Relative Translational Energy (E_{trans}), in kcal mol⁻¹ for the Products of the Hydrogen Elimination Pathway^a

velocity (km s ⁻¹)	potential	H elimination		
		$\langle E_{\text{vib}} \rangle$	$\langle E_{\text{rot}} \rangle$	$\langle E_{\text{trans}} \rangle$
8	AM1	78.1 (0.62)	22.9 (0.18)	23.9 (0.19)
	AM1-SRP1	73.9 (0.67)	17.1 (0.16)	18.8 (0.17)
	AM1-SRP2	84.0 (0.63)	29.4 (0.22)	20.7 (0.15)
10	AM1	115.9 (0.59)	47.6 (0.24)	32.3 (0.17)
	AM1-SRP1	115.4 (0.63)	43.4 (0.24)	23.3 (0.13)
	AM1-SRP2	129.2 (0.65)	44.6 (0.22)	25.9 (0.13)

^aThe fraction of the total energy (initial translational energy + the average of the reaction enthalpies) is given in parentheses.

Table 5. Average Total Vibrational Energy (E_{vib}) Excluding Zero Point, Rotational (E_{rot}), and Relative Translational Energy (E_{trans}), in kcal mol⁻¹ for the Products of the Methyl Elimination Pathway^a

velocity (km s ⁻¹)	potential	CH ₃ elimination		
		$\langle E_{\text{vib}} \rangle$	$\langle E_{\text{rot}} \rangle$	$\langle E_{\text{trans}} \rangle$
8	AM1	66.3 (0.52)	14.0 (0.11)	48.1 (0.38)
	AM1-SRP1	61.9 (0.49)	14.4 (0.11)	49.1 (0.39)
	AM1-SRP2	60.4 (0.48)	17.4 (0.14)	47.5 (0.38)
10	AM1	97.6 (0.55)	17.9 (0.10)	62.0 (0.35)
	AM1-SRP1	94.1 (0.52)	22.5 (0.12)	64.1 (0.35)
	AM1-SRP2	109.6 (0.58)	26.7 (0.14)	50.1 (0.27)

^aThe fraction of the total energy (initial translational energy + the average of the reaction enthalpies) is given in parentheses.

each reaction pathway are averaged together. In Tables 3–5, we also give the fraction of total energy deposited in vibration, rotation, and translation in parentheses. The total energy is defined by the sum of the collision energy and the average enthalpy of the reaction. For H-atom elimination, an unusually large amount of the total energy (about 80%) goes into internal energy of the product DMMP–O radical. For CH₃ elimination 60–70% goes into product internal energy, and for H-atom abstraction between 50 and 60% goes into product internal energy. For the elimination reactions, most of this internal excitation goes into vibration. As previously observed in the literature,^{12,17} H-abstraction at these velocities occurs by a “stripping” mechanism involving glancing collisions. H-abstraction therefore does not redistribute much of the available energy into internal excitation, whereas H-elimination and to a lesser extent CH₃ elimination involve low-impact parameter, or “hard”, collisions. Through an examination of the opacity function $P(b)$, these mechanisms are readily apparent. The opacity function has the following relation to the total reactive cross section, $\sigma = 2\pi \int_0^{b_{\max}} P(b)b db$, where b is the impact parameter. Figure 6 shows the opacity function for the three different reaction channels at 10 km s⁻¹ using the AM1-SRP1 surface. The internal energy deposition is correlated with the distribution of impact parameters: nearly all H-elimination reactions (red) are hard collisions with impact parameters less than 1.0 Å. Nearly all CH₃ elimination reactions occur for impact parameters less than 2 Å, and the H-atom abstraction pathway has a broad range of impact parameters, mostly weighted between 2 and 3 Å.

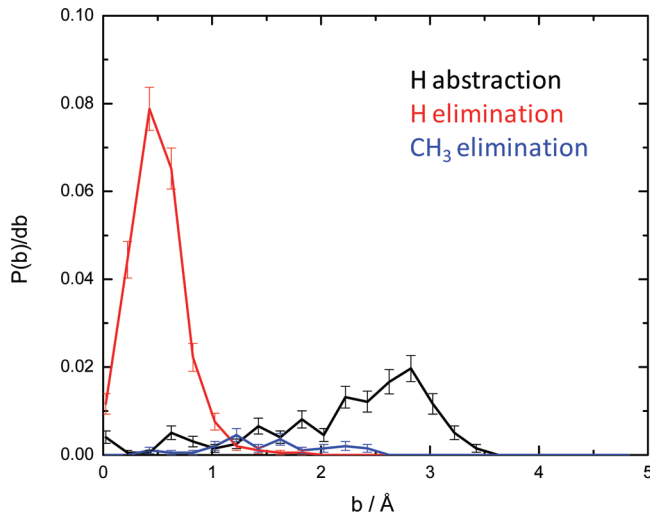


Figure 6. Opacity function divided by the bin width, $P(b)/db$, in units of (1/Å) calculated at a collision velocity of 10 km s⁻¹ using the AM1-SRP1 potential. The hydrogen abstraction reaction is shown in black, the hydrogen elimination reaction is shown in red, and the methyl elimination reaction is shown in blue. Error bars indicate standard deviation, and the impact parameter, b , bin size is 0.2 Å.

Nonreactive collisional excitation of DMMP leads to cross sections much larger than reactive pathways and may carry important collision dynamics information. For the nonreactive collision process, flux–velocity maps provide insight into the energy transfer process. Figure 7 shows flux–velocity contour maps for nonreactive collisions of O(³P) + DMMP at velocities of 4, 6, 8, and 10 km s⁻¹ using the AM1-SRP1 Hamiltonian. For reference, inner and outer circles are shown at 5 and 10 km s⁻¹, respectively. Forward scattering (zero-degree scattering angle) points to the right, and the contour color is on a log scale to bring out important features. From these features, there are two main scattering mechanisms, a dominant forward scattering component with little internal excitation and a lesser but significant side and backscatter component which leads to internal excitation. In addition, there is a third mechanism at low scattering angles at 8 and 10 km s⁻¹, which corresponds to large DMMP internal energies. This may correspond to O-atoms undergoing low-impact parameter collisions that get funneled into the forward scattering direction.

Vibrational Cross Sections. For H-atom abstraction, the OH vibrational state cross section is plotted in Figure 8 at the AM1, SRP1, and SRP2 levels at collision velocities of 6, 8, and 10 km s⁻¹. The abstraction reactions from the AM1 calculations result in the most vibrationally excited OH, which is consistent with the overly large exothermicities at this level of theory. For SRP1 and SRP2, the OH vibrational distributions peak at $n = 1$. These vibrational distributions remain fairly constant over a broad range of collision velocities.

For H-abstraction, the DMMP radical product internal energy vibrational and rotational cross sections at 6, 8, and 10 km s⁻¹ are shown in Figure 9 at the AM1, SRP1, and SRP2 levels of theory. Zero-point energy is subtracted from the vibrational binning in order to isolate product internal energy change. We have also plotted DMMP radical vibrational thermal distributions, scaled by the total reaction cross section. For 6 km s⁻¹, the distributions plotted are 800 K (AM1), 900 K (AM1-SRP1), and 800 K (AM1-SRP2); for 8 km s⁻¹, the distributions plotted are 900 K (AM1), 1000 K (AM1-SRP1),

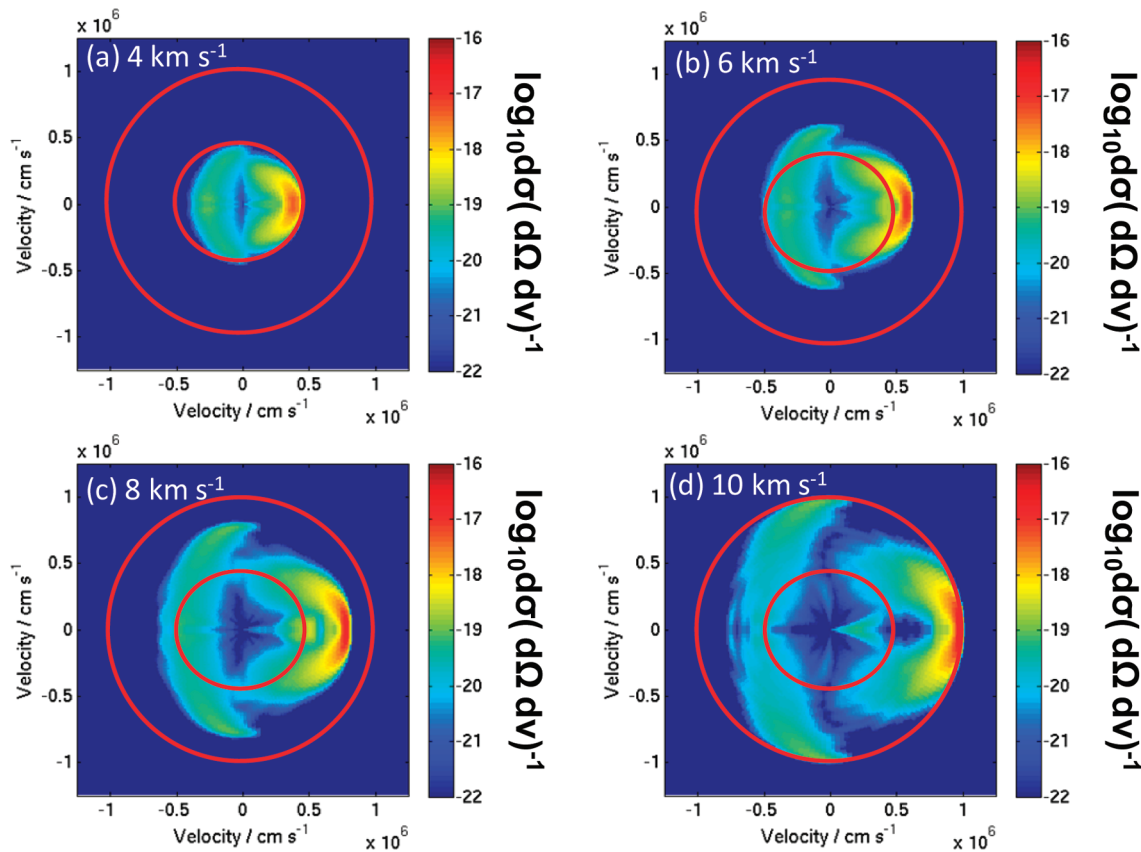


Figure 7. Velocity–flux contours $\log_{10} d\sigma(d\Omega dv)^{-1}$ in units of $\text{cm}^2 (\text{sr cm s}^{-1})^{-1}$ for the differential cross section of nonreactive collisions of DMMP + O(³P) at (a) 4, (b) 6, (c) 8, and (d) 10 km s^{-1} . The results are shown for the AM1-SRP1 potential.

and 800 K (AM1-SRP2); and for 10 km s^{-1} , the distributions plotted are 900 K (AM1), 900 K (AM1-SRP1), and 900 K (AM1-SRP2). These thermal distributions fit the calculated distributions fairly well, except for indications of a high-energy tail at the higher velocities. For the AM1-SRP1, the vibrational distribution is shifted to a higher energy which is particularly noticeable at a collision velocity of 8 km s^{-1} and is consistent with the average internal energy values in Table 3.

The vibrational cross sections of the DMMP–O radical following hydrogen elimination at 8 and 10 km s^{-1} are shown in Figure 10. Zero-point energy is subtracted from the vibrational binning in order to isolate product internal energy change. Thermal vibrational distributions (scaled by the cross section) are plotted with dashed curves. At 8 km s^{-1} , distributions of 1700 K (AM1), 1600 K (AM1-SRP1), and 1700 K (AM1-SRP2) are plotted. The thermal distributions plotted for 10 km s^{-1} are 2200 K (AM1), 2200 K (AM1-SRP1), and 2200 K (AM1-SRP2). The vibrational cross sections for the DMMP–O radical product are well fit by the thermal distributions, which correspond to extremely high temperatures, and strongly depend on the collision energy. These high temperature fits are consistent with the large average internal energy values of Table 4. Vibrational cross sections for methyl elimination products were not examined due to the insufficient number of methyl elimination reactions to generate significant distribution statistics.

To characterize the nonreactive distributions, in Figure 11 we show the vibrational cross sections versus DMMP internal energy at 4, 8, and 10 km s^{-1} for the nonreactive collision case, where we have subtracted the initial DMMP zero-point energy.

Following the analysis of the flux velocity maps of Figure 7, where forward and backward scattering mechanisms were found, we decompose the cross sections into angular scattering components. At 4 km s^{-1} , the distribution is divided into scattering between 5° and 70° and scattering greater than 70°. At 8 and 10 km s^{-1} , the distribution is divided into three parts: 5–20°, 20–70°, and 70–180°. For reference, thermal vibrational distributions of DMMP are shown in the plots with dashed lines and are scaled by the cross section at a particular range of scattering angles. For all velocities the large-angle scattering component (70–180°) agrees well with thermal distributions at 400, 1200, and 1600 K for the 4, 8, and 10 km s^{-1} collision velocities, respectively. At 8 and 10 km s^{-1} , the agreement of the 20–70° component with lower temperature thermal distributions is not as good, with a high-energy tail in the calculated results that is not accounted for.

Rotational Cross Sections of Reactive Collisions. For the H-atom abstraction channel, the rotational state cross sections for OH at velocities of 6, 8, and 10 km s^{-1} are plotted in Figure 12a, b, and c, respectively. The average rotational energy increases and the rotational distributions widen modestly with collision velocity. Unlike the vibrational cross sections, the rotational cross sections did not fit Boltzmann distributions well. Therefore, to characterize the rotational distributions, we fit the rotational energy cross sections to distributions derived from surprisal theory³⁶

$$\sigma(E_{\text{rot}}) \propto \sigma^0(E_{\text{rot}}) \exp(-\theta f_{\text{rot}})$$

where the prior distribution, σ^0 , is proportional to $(2j+1)(E_{\text{tot}} - E_{\text{rot}})^{1/2}$, f_{rot} is the energy fraction in rotation, and θ is the

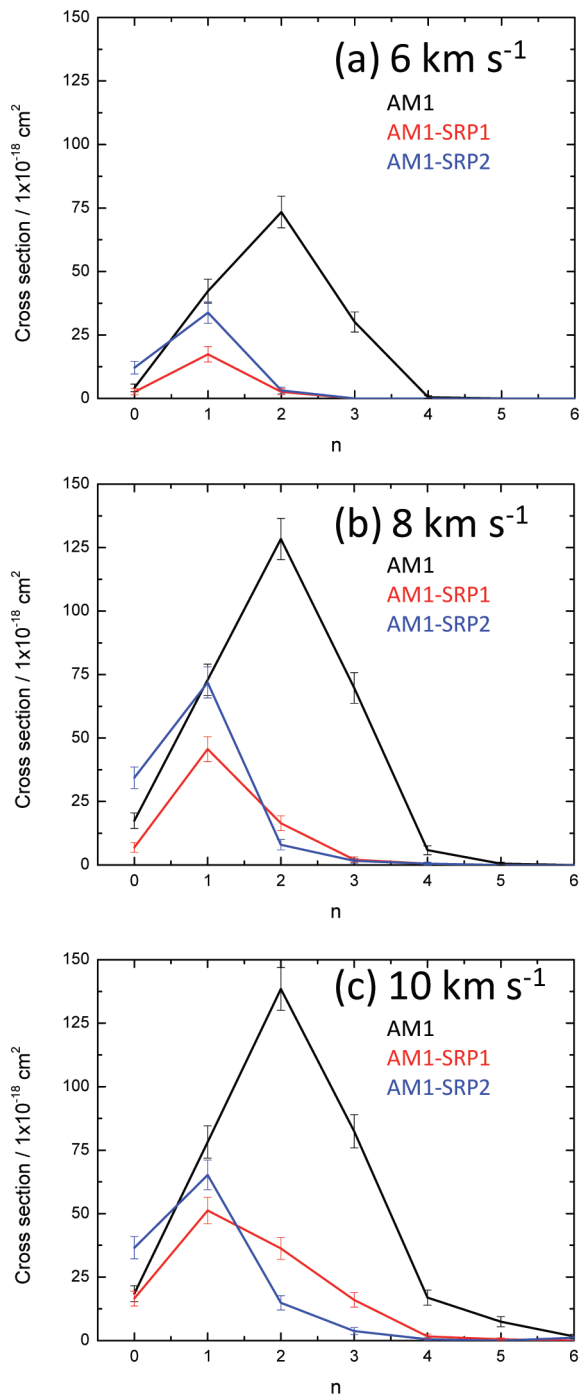


Figure 8. Vibrational state cross sections for the OH product using AM1 (black), AM1-SRP1 (red), and AM1-SRP2 (blue) at collision velocities of (a) 6, (b) 8, and (c) 10 km s^{-1} . Error bars indicate standard deviation.

surprisal parameter. These fits are shown in dashed curves in Figure 12 for the OH product of the hydrogen abstraction reactions. For the OH product, the surprisal parameters are similar for all the potentials.

For the H-abstraction channel, the rotational cross sections for the residual DMMP radical product are given in Figure 13a–c for collision velocities of 6, 8, and 10 km s^{-1} . The AM1 rotational distributions are generally more excited than the SRP distributions. This is probably due to errors in the AM1 potential in the product channel leading to overly large AM1

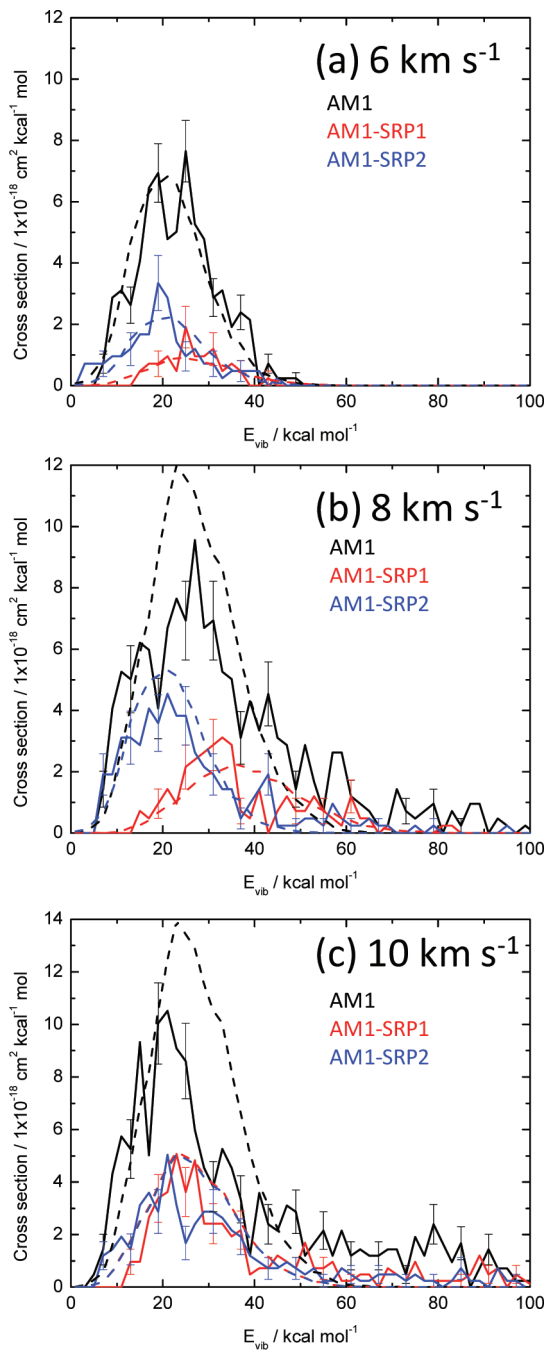


Figure 9. Vibration cross sections as a function of vibrational energy in kcal mol^{-1} for the residual DMMP radical product following hydrogen abstraction using AM1 (black), AM1-SRP1 (red), and AM1-SRP2 (blue) at collision velocities of (a) 6, (b) 8, and (c) 10 km s^{-1} . The dashed curves are thermal distributions and for comparison are scaled by the abstraction reaction cross section for AM1 (black), AM1-SRP1 (red), and AM1-SRP2 (blue), respectively. For 6 km s^{-1} , thermal distributions of 800 K (AM1), 900 K (AM1-SRP1), and 800 K (AM1-SRP2) are shown. For 8 km s^{-1} , thermal distributions of 900 K (AM1), 1000 K (AM1-SRP1), and 800 K (AM1-SRP2) are shown. For 10 km s^{-1} , thermal distributions of 900 K (AM1), 900 K (AM1-SRP1), and 900 K (AM1-SRP2) are shown. In all plots, error bars which indicate standard deviation are given for every third data point, and 2 kcal mol^{-1} energy bins are used.

exothermicities. The SRP-1 cross section at low rotational energies is also significantly larger than the SRP-2 cross section. This reflects a qualitative difference between the two surfaces

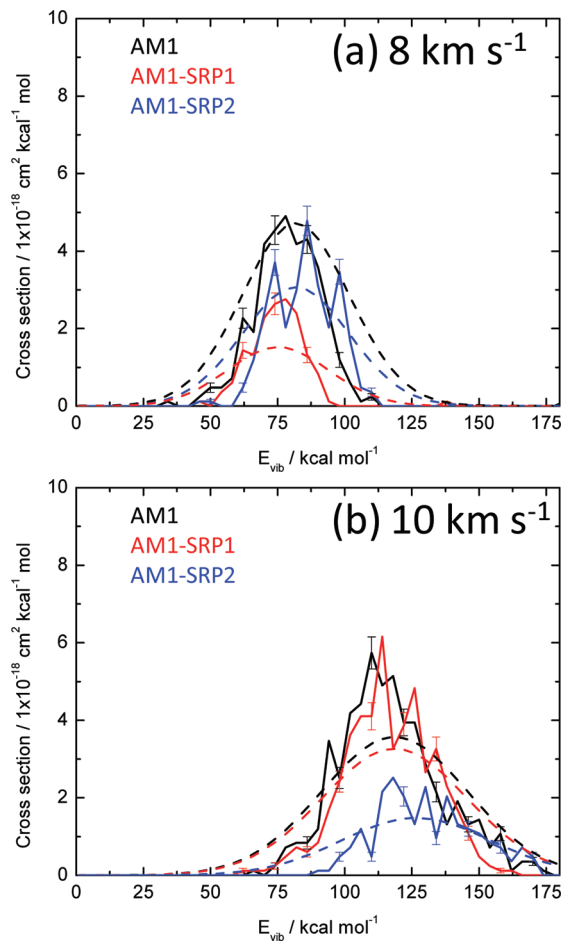


Figure 10. Vibration cross sections as a function of energy in kcal mol^{-1} for the residual DMMP product following hydrogen elimination using AM1 (black), AM1-SRP1 (red), and AM1-SRP2 (blue) at collision velocities of (a) 8 and (b) 10 km s^{-1} . The dashed curves are thermal distributions and for comparison are scaled by the elimination reaction cross section for the AM1 (black), AM1-SRP1 (red), and AM1-SRP2 (blue), respectively. For 8 km s^{-1} , thermal distributions of 1700 K (AM1), 1600 K (AM1-SRP1), and 1700 K (AM1-SRP2) are shown. For 10 km s^{-1} , thermal distributions of 2200 K (AM1), 2200 K (AM1-SRP1), and 2200 K (AM1-SRP2) are shown. In all plots, error bars which indicate standard deviation are given for every third data point, and 4 kcal mol^{-1} energy bins are used.

seen also in the vibrational distributions and internal energies. The AM1-SRP2 surface is a better overall fit to the benchmark CBS-QB3 results for this pathway, as indicated in Table 2, and we believe the AM1-SRP2 cross sections are likely more accurate. The surprisal fits of the rotational distributions are shown as dashed lines in Figure 13. In this case, the prior distributions were obtained by modeling the DMMP radical as an asymmetric top and determining the rotational degeneracy as a function of rotational energy. The surprisal parameter values for the unmodified AM1 and AM1-SRP1 are similar. The surprisal parameter values for the AM1-SRP2 fits are nearly three times greater than both the unmodified AM1 and AM1-SRP1 parameters. The rotational cross sections are given for the DMMP–O radical product following H-elimination at 8 and 10 km s^{-1} in Figure 14a and b, respectively. There is a broad distribution of rotational energies, reflecting the unusually large deposition of initial translation into internal energy. The surprisal fits plotted in Figure 14 as dashed lines

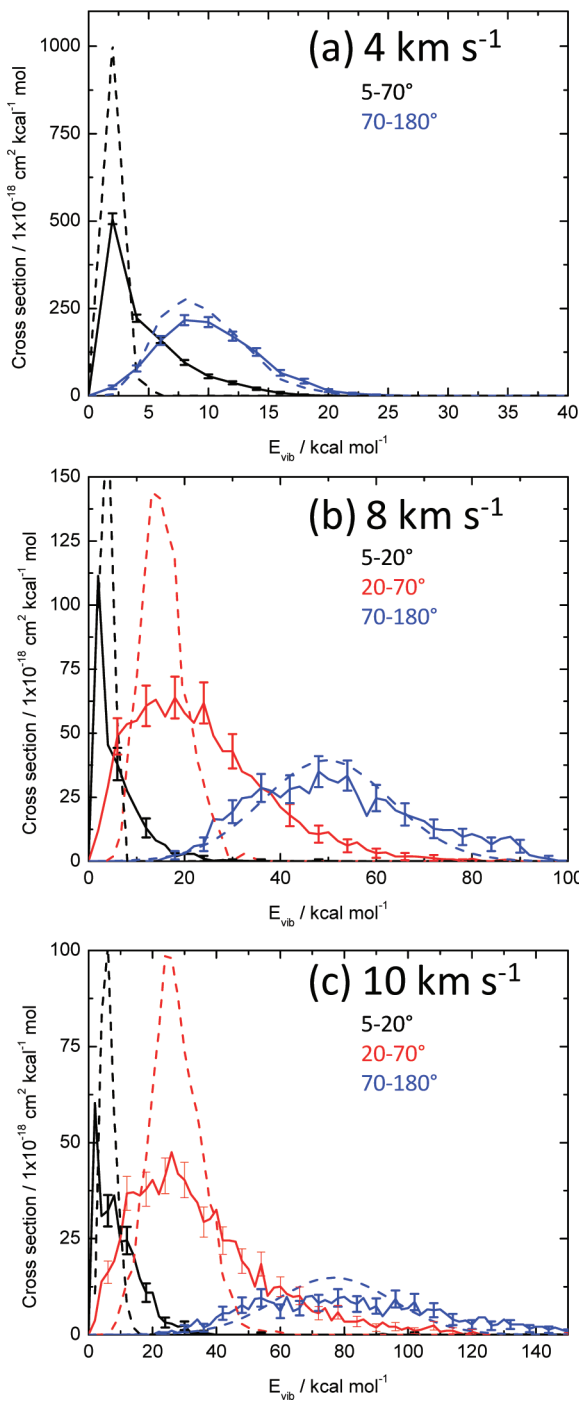


Figure 11. Vibrational cross sections as a function of energy in kcal mol^{-1} for DMMP following a nonreactive collision at (a) 4, (b) 8, and (c) 10 km s^{-1} using AM1-SRP1. The distribution at 4 km s^{-1} is separated into two distributions, $5-70^\circ$ (black) and $70-180^\circ$ (blue), while the distributions at 8 and 10 km s^{-1} are separated into three distributions, $5-20^\circ$ (black), $20-70^\circ$ (red), and $70-180^\circ$ (blue). The dashed curves are thermal distributions scaled by the inelastic cross section for the angular distributions. For 4 km s^{-1} , thermal distributions of 100 K ($5-70^\circ$) and 400 K ($70-180^\circ$) are shown. For 8 km s^{-1} , thermal distributions of 200 K ($5-20^\circ$), 600 K ($20-70^\circ$), and 1200 K ($70-180^\circ$) are shown. For 10 km s^{-1} , thermal distributions of 300 K ($5-20^\circ$), 800 K ($20-70^\circ$), and 1600 K ($70-180^\circ$) are shown. In all plots error bars which indicate standard deviation are given for every third data point, and 2 kcal mol^{-1} energy bins are used.

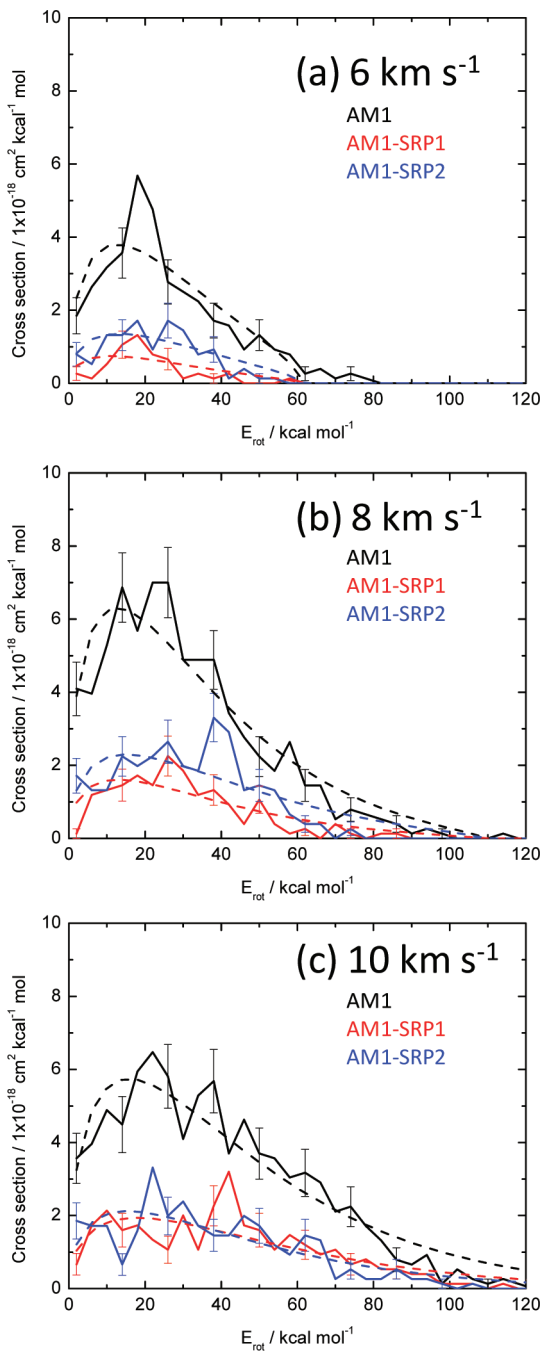


Figure 12. Rotational state cross sections as a function of energy in kcal mol^{-1} for the OH product using AM1 (black), AM1-SRP1 (red), and AM1-SRP2 (blue) at collision velocities of (a) 6, (b) 8, and (c) 10 km s^{-1} . The dashed curves are surprisal fits for the rotational distributions: (a) $\theta_{\text{AM1}} = 1.7$, $\theta_{\text{AM1-SRP1}} = 2.0$, $\theta_{\text{AM1-SRP2}} = 1.6$; (b) $\theta_{\text{AM1}} = 3.5$, $\theta_{\text{AM1-SRP1}} = 3.4$, $\theta_{\text{AM1-SRP2}} = 2.8$; (c) $\theta_{\text{AM1}} = 4.6$, $\theta_{\text{AM1-SRP1}} = 4.0$, $\theta_{\text{AM1-SRP2}} = 4.7$. In all plots, error bars which indicate standard deviation are given for every third data point, and 4 kcal mol^{-1} energy bins are used.

for each potential are similar for all three potentials. As with the vibrational distributions, the methyl elimination rotational distribution statistics were too poor to effectively analyze.

DMMP Spectra. Optical detection of $\text{O}(\text{P}) + \text{DMMP}$ nonreactive collisions may be an important probe in future hyperthermal beam measurements. As suggested by Figures 7 and 11 and in analysis of the nonreacted rotational distributions

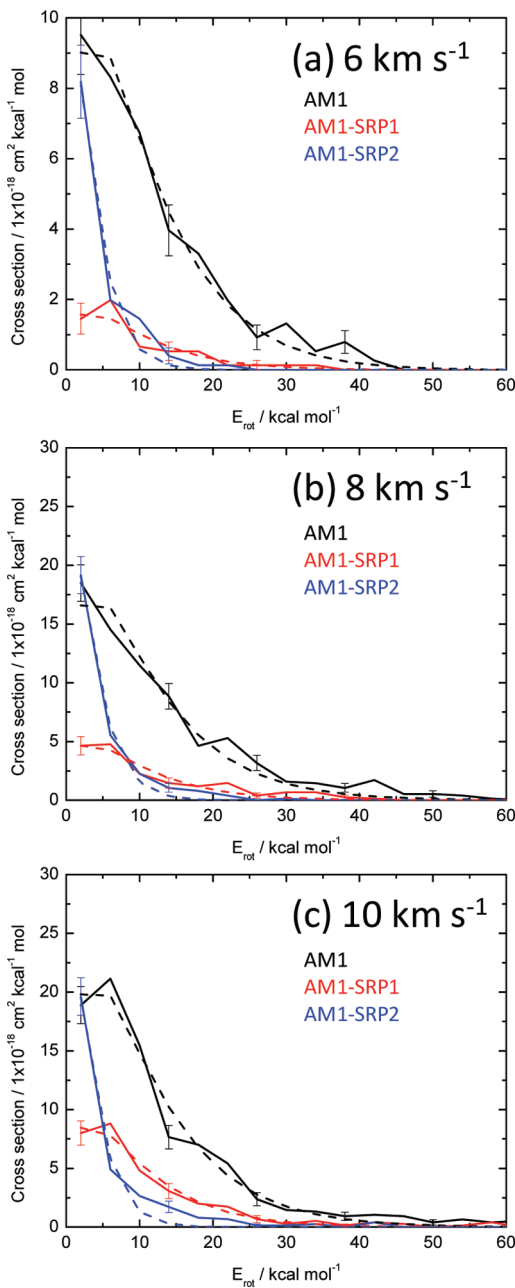


Figure 13. Rotational cross sections as a function of energy in kcal mol^{-1} for the residual DMMP radical product following hydrogen abstraction using AM1 (black), AM1-SRP1 (red), and AM1-SRP2 (blue) at collision velocities of (a) 6, (b) 8, and (c) 10 km s^{-1} . The dashed curves are surprisal fits for the rotational distributions: (a) $\theta_{\text{AM1}} = 7.7$, $\theta_{\text{AM1-SRP1}} = 8.6$, $\theta_{\text{AM1-SRP2}} = 25.3$; (b) $\theta_{\text{AM1}} = 13.9$, $\theta_{\text{AM1-SRP1}} = 15.9$, $\theta_{\text{AM1-SRP2}} = 44.4$; (c) $\theta_{\text{AM1}} = 21.9$, $\theta_{\text{AM1-SRP1}} = 25.1$, $\theta_{\text{AM1-SRP2}} = 72.8$. In all plots, error bars which indicate standard deviation are given for every third data point, and 4 kcal mol^{-1} energy bins are used.

which we have not shown, product internal excitation will be sensitive to the scattering angle and can be characterized to some extent by a Boltzmann temperature. High-temperature spectra of DMMP are not available. Therefore, we have simulated DMMP at several representative temperatures (298, 800, and 1600 K) which span the general expected range of the product distributions. These spectra are plotted in Figure 15. They were obtained by a Monte Carlo technique which uses known dipole transition moments and other spectroscopic

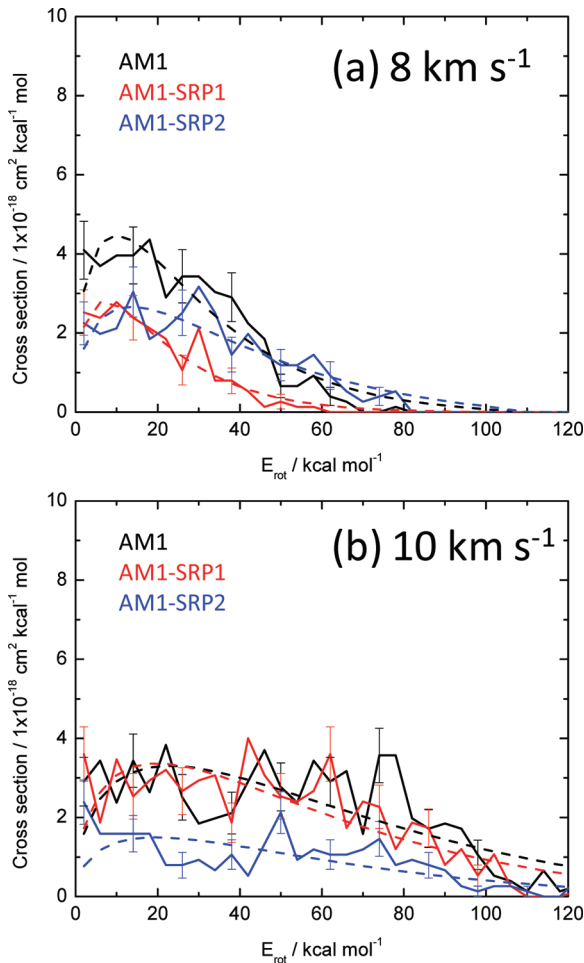


Figure 14. Rotational cross sections as a function of energy in kcal mol^{-1} for the residual DMMP product following hydrogen elimination using AM1 (black), AM1-SRP1 (red), and AM1-SRP2 (blue) at collision velocities of (a) 8 and (b) 10 km s^{-1} . The dashed curves are surprisal fits for the rotational distributions: (a) $\theta_{\text{AM1}} = 4.7$, $\theta_{\text{AM1-SRP1}} = 6.8$, $\theta_{\text{AM1-SRP2}} = 3.2$; (b) $\theta_{\text{AM1}} = 2.9$, $\theta_{\text{AM1-SRP1}} = 3.5$, $\theta_{\text{AM1-SRP2}} = 3.6$. In all plots, error bars which indicate standard deviation are given for every third data point, and 4 kcal mol^{-1} energy bins are used.

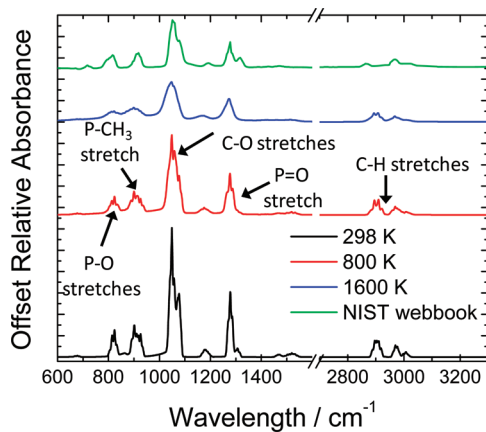


Figure 15. Calculated spectra of DMMP with $T = 298 \text{ K}$ (black), $T = 800 \text{ K}$ (red), and $T = 1600 \text{ K}$ (blue). The spectrum from the NIST database at 373 K is also shown (green).

information to generate representative spectral lines.³⁷ Large numbers of individual ro-vibrational line shapes are generated,

typically tens of thousands, depending on temperature. These representative lines are weighted in a Monte Carlo fashion, and each vibrational band is scaled by its dipole strength. A spectrum is built up which yields a representation of the true spectrum which can contain millions of lines or more. The DMMP 373 K spectrum from the NIST database³⁸ is also plotted in Figure 15 for comparison. The calculated spectra are normalized by the integrated intensity of the NIST spectrum. Additionally, the vibrational modes with strong features are indicated in the figure. As expected, the spectrum broadens with temperature. As indicated in the figure, a measurement of the spectral peak widths in a crossed-beam apparatus should yield an estimate of the nonreactive collision product temperatures.

IV. CONCLUSIONS

We developed two global potential energy surfaces for $\text{O}^{(3P)} + \text{DMMP}$ collisions, using the specific reaction parameters (SRP) approach. Each global surface is simultaneously fit along the three major reaction pathways: hydrogen abstraction, hydrogen elimination, and methyl elimination. We used these global potential surfaces in classical dynamics simulations and computed reactive cross sections from 4 to 10 km s^{-1} collision velocity. We examined the energy disposal and angular distributions of the reactive and nonreactive collided products. We found that for reactive collisions, an unusually large amount of the initial collision energy is transformed into internal energy. We also found that internal energy deposition is correlated with the distribution of impact parameters: nearly all H-elimination reactions are hard collisions with impact parameters less than 1.0 \AA , and about 80% of available energy is deposited in the internal energy of the products. Nearly all CH_3 elimination reactions occur for impact parameters less than 2 \AA and result in about 60–70% of available energy turning into internal energy, and the H-atom abstraction pathway has a broad range of impact parameters up to about 3 \AA and results in about 50–60% of available energy transformed into internal product energy. For the elimination reactions, most of this internal excitation goes into vibration. We also analyzed the nonreactive and reactive product internal energy distributions, many of which fit Boltzmann temperatures up to $\sim 2000 \text{ K}$, and predict excited product spectra.

■ AUTHOR INFORMATION

Notes

The authors declare no competing financial interest.

■ ACKNOWLEDGMENTS

This work was supported by a DTRA/JSTO basic research program award, BRCALL07-N-2-0029. M.B. and P.F.C. acknowledge support under Contract No. FA8718-05-C-0077.

■ REFERENCES

- (1) Bermudez, V. M. *J. Phys. Chem. C* **2010**, *114*, 3063–3074.
- (2) Quenneville, J.; Taylor, R. S.; van Duin, A. C. T. *J. Phys. Chem. C* **2010**, *114*, 18894–18902.
- (3) Yang, L.; Shroll, R. M.; Zhang, J. X.; Lourderaj, U.; Hase, W. L. *J. Phys. Chem. A* **2009**, *113*, 13762–13771.
- (4) Panayotov, D. A.; Morris, J. R. *J. Phys. Chem. C* **2009**, *113*, 15684–15691.
- (5) Conforti, P. F.; Braunstein, M.; Dodd, J. A. *J. Phys. Chem. A* **2009**, *113*, 13752–13761.

- (6) Sheinker, V. N.; Mitchell, M. B. *Chem. Mater.* **2002**, *14*, 1257–1268.
- (7) Korobkinichev, O. P.; Ilyin, S. B.; Bolshova, T. A.; Shvartsberg, V. M.; Chernov, A. A. *Combust. Flame* **2000**, *121*, 593–609.
- (8) Glaude, P. A.; Curran, H. J.; Pitz, W. J.; Westbrook, C. K. *Proc. Comb. Inst.* **2000**, *28*, 1749–1756.
- (9) Glaude, P. A.; Melius, C.; Pitz, W. J.; Westbrook, C. K. *Proc. Comb. Inst.* **2002**, *29*, 2469–2476.
- (10) Troya, D.; Pascual, R. Z.; Garton, D. J.; Minton, T. K.; Schatz, G. C. *J. Phys. Chem. A* **2003**, *107*, 7161–7169.
- (11) Troya, D.; Pascual, R. Z.; Schatz, G. C. *J. Phys. Chem. A* **2003**, *107*, 10497–10506.
- (12) Yan, T. Y.; Doubleday, C.; Hase, W. L. *J. Phys. Chem. A* **2004**, *108*, 9863–9875.
- (13) Gonzales-Lafont, A.; Truong, T. N.; Truhlar, D. G. *J. Phys. Chem.* **1991**, *95*, 4618–4627.
- (14) Troya, D.; Schatz, G. Dynamics Studies of the O (3P) + CH₄, C₂H₆, and C₃H₈ Reactions. In *Theory of Chemical Reaction Dynamics*; Lagana, A., Lendvay, G., Eds.; Kluwer Academic Publishers: New York, 2005; Vol. 145, pp 329–348.
- (15) Garton, D. J.; Minton, T. K.; Troya, D.; Pascual, R.; Schatz, G. *C. J. Phys. Chem. A* **2003**, *107*, 4583–4587.
- (16) Zhang, J. M.; Upadhyaya, H. P.; Brunsvoold, A. L.; Minton, T. K. *J. Phys. Chem. B* **2006**, *110*, 12500–12511.
- (17) Troya, D.; Garcia-Molina, E. *J. Phys. Chem. A* **2005**, *109*, 3015–3023.
- (18) Braams, B. J.; Bowman, J. M. *Int. Rev. Phys. Chem.* **2009**, *28*, 577–606.
- (19) Castillo, J. F.; Aoiz, F. J.; Banares, L. *J. Chem. Phys.* **2006**, *125*, 124316.
- (20) Chen, C.; Shepler, B. C.; Braams, B. J.; Bowman, J. M. *Phys. Chem. Chem. Phys.* **2009**, *11*, 4722–4727.
- (21) Conforti, P. F.; Braunstein, M.; Braams, B. J.; Bowman, J. M. *J. Chem. Phys.* **2010**, *133*, 164312.
- (22) Ischtwan, J.; Collins, M. A. *J. Chem. Phys.* **1994**, *100*, 8080–8088.
- (23) Martinez-Nunez, E.; Vazquez, S. A.; Aoiz, F. J.; Castillo, J. F. *J. Phys. Chem. A* **2006**, *110*, 1225–1231.
- (24) Park, W. K.; Park, J.; Park, S. C.; Braams, B. J.; Chen, C.; Bowman, J. M. *J. Chem. Phys.* **2006**, *125*, 081101.
- (25) Doubleday, C. *J. Phys. Chem. A* **2001**, *105*, 6333–6341.
- (26) Doubleday, C.; Nendel, M.; Houk, K. N.; Thweatt, D.; Page, M. *J. Am. Chem. Soc.* **1999**, *121*, 4720–4721.
- (27) Layfield, J. P.; Sweeney, A. F.; Troya, D. *J. Phys. Chem. A* **2009**, *113*, 4294–4304.
- (28) More, J. J.; Garbow, B. S.; Hillstrom, K. E. User Guide for MINPACK-1, Argonne National Laboratory, Lemont, IL, 1980.
- (29) Schmidt, M. W.; Baldridge, K. K.; Boatz, J. A.; Elbert, S. T.; Gordon, M. S.; Jensen, J. H.; Koseki, S.; Matsunaga, N.; Nguyen, K. A.; Su, S. J.; et al. *J. Comput. Chem.* **1993**, *14*, 1347–1363.
- (30) Rossi, I.; Truhlar, D. G. *Chem. Phys. Lett.* **1995**, *233*, 231–236.
- (31) Doubleday, C. *J. Phys. Chem. A* **2001**, *105*, 6333–6341.
- (32) Sullivan, P. A.; Sumathi, R.; Green, W. H.; Tester, E. W. *Phys. Chem. Chem. Phys.* **2004**, *6*, 4296–4309.
- (33) Frisch, M. J.; Trucks, G. W.; Schlegel, H. B.; Scuseria, G. E.; Robb, M. A.; Cheeseman, J. R.; Montgomery, J. A., Jr.; Vreven, T.; Kudin, K. N.; Burant, J. C.; et al. *Gaussian 03*, revision C.02; Gaussian, Inc.: Wallingford, CT, 2003.
- (34) Brunsvoold, A. L.; Upadhyaya, H. P.; Zhang, J.; Cooper, R.; Minton, T. K.; Braunstein, M.; Duff, J. W. *J. Phys. Chem. A* **2008**, *112*, 2192–2205.
- (35) Murad, E. *J. Spacecraft Rockets* **1996**, *33*, 131–136.
- (36) Levine, R. D.; Bernstein, R. B. *Molecular Reaction Dynamics and Chemical Reactivity*; Oxford University Press: New York, 1987.
- (37) Sundberg, R. L.; Bernstein, L. S.; Duff, J. W. *J. Spacecraft Rockets* **1993**, *30*, 731–741.
- (38) NIST. NIST Chemistry Webbook.